

Lattice dynamics and the electron-phonon interaction in Ca_2RuO_4

H. Rho,^{1,2} S. L. Cooper,² S. Nakatsuji,³ H. Fukazawa,³ and Y. Maeno,^{3,4}

¹*Department of Physics, Chonbuk National University, Jeonju 561-756, Korea*

²*Department of Physics and Frederick Seitz Materials Research Laboratory, University of Illinois at Urbana-Champaign, Urbana, Illinois 61801*

³*Department of Physics, Kyoto University, Kyoto 606-8502, Japan*

⁴*International Innovation Center, Kyoto University, Kyoto 606-8501, Japan*

(Dated: November 12, 2018)

We present a Raman scattering study of Ca_2RuO_4 , in which we investigate the temperature-dependence of the lattice dynamics and the electron-phonon interaction below the metal-insulator transition temperature (T_{MI}). Raman spectra obtained in a backscattering geometry with light polarized in the *ab*-plane reveal $9B_{1g}$ phonon modes (140, 215, 265, 269, 292, 388, 459, 534, and 683 cm^{-1}) and $9A_g$ phonon modes (126, 192, 204, 251, 304, 322, 356, 395, and 607 cm^{-1}) for the orthorhombic crystal structure ($\text{Pbca}-D_{2h}^{15}$). With increasing temperature toward T_{MI} , the observed phonon modes shift to lower energies and exhibit reduced spectral weights, reflecting structural changes associated with the elongation of the RuO_6 octahedra. Interestingly, the phonons exhibit significant increases in linewidths and asymmetries for $T > T_{\text{N}}$. These results indicate that there is an increase in the effective number of electrons and the electron-phonon interaction strengths as the temperature is raised through T_{N} , suggesting the presence of orbital fluctuations in the temperature regime $T_{\text{N}} < T < T_{\text{MI}}$.

PACS numbers: 75.30.-m, 75.50.Ee, 78.30.-j, 71.30.+h

I. INTRODUCTION

Like many other transition-metal oxides that exhibit strong correlations among spin, charge, orbital, and lattice degrees of freedom, $\text{Ca}_{2-x}\text{Sr}_x\text{RuO}_4$ exhibits many exotic phenomena throughout its rich phase diagram.^{1,2,3,4,5,6,7,8,9,10,11} For instance, not only do the ruthenates exhibit orbital ordering,^{5,6,7,8} but also orbital-dependent superconductivity, heavy-mass Fermi liquid behavior, and metal-insulator transitions.^{1,2,4}

The single-layer ruthenate material Sr_2RuO_4 is a superconductor below $T_c = 1.5\text{ K}$, possibly with an unconventional *p*-wave pairing state.¹² Substitution of Ca for Sr significantly distorts the lattice structure and lowers the crystal symmetry from cubic to orthorhombic, giving rise to remarkable changes in magnetic, electronic, and structural properties.^{2,4,13} The ground state of Ca_2RuO_4 is antiferromagnetic (AF) insulating.^{14,15} With increasing temperature, Ca_2RuO_4 becomes paramagnetic (PM) insulating at $T_{\text{N}} = 113\text{ K}$ and then PM metallic at $T_{\text{MI}} = 357\text{ K}$.^{2,15,16} The metal-insulator (MI) transition is first-order, as evidenced by the observation of thermal hysteresis. Further, the transition is driven by an elongation of the RuO_6 octahedra with increasing temperature through T_{MI} , and therefore the insulating and metallic states are characterized by short (S-Pbca) and long (L-Pbca) *c*-axis lattice parameters, respectively.^{13,17} As a function of Sr-substitution, *x*, the AF ground state of $\text{Ca}_{2-x}\text{Sr}_x\text{RuO}_4$ persists for $x < 0.2$. Sr substitution changes both T_{N} and T_{MI} , and significantly affects magnetic, electronic, orbital, and structural correlations in this material. For instance, Raman scattering results obtained on $\text{Ca}_{2-x}\text{Sr}_x\text{RuO}_4$ have shown that Sr substitution causes a dramatic increase in the renormalization of

the two-magnon (2M) energy and linewidth, and an increase of the electron-phonon interaction strength.¹⁰ Raman scattering measurements further suggest that the exchange coupling constant *J* in $\text{Ca}_{2-x}\text{Sr}_x\text{RuO}_4$ is relatively insensitive to pressure⁹ and Sr content.¹⁰

Other complex oxides are known to exhibit significant changes in phonon dynamics near important phase transitions. For example, $\text{La}_{0.7}\text{Ca}_{0.3}\text{MnO}_3$ displays a significant shift of the transverse optical phonon energy near the MI transition, giving rise to an increased electron-phonon interaction related to changes in the lattice parameters.¹⁸ Raman studies of LaMnO_3 reveal an effect of the spin-lattice interaction near the transition to AF order.¹⁹ In $\text{La}_{2-x}\text{Sr}_x\text{CuO}_4$, an increase of Sr concentration causes the appearance of an asymmetric phonon lineshape and a dramatic decrease of the phonon intensity associated with the apical oxygen vibration, indicating that the electron-phonon interaction is also important in this material.²⁰ Inelastic neutron scattering and x-ray scattering studies have suggested the presence of orbital fluctuations in LaTiO_3 .²¹ As described in Ref. 21, an electronic continuum and anomalous phonon behavior with a Fano profile observed in the Raman response of $R\text{TiO}_3$ (*R*=rare earth)²² may also indicate the presence of orbital fluctuations in the insulating region of this system. Therefore, it is of great interest to study how spin, charge, orbital, and lattice correlations evolve in Ca_2RuO_4 through different phase transitions, particularly as a means of comparing the exotic properties of this system to those of complex oxides such as the cuprates, manganites, and titanates. In this paper, we use the unique strengths of Raman scattering to explore lattice dynamics and the electron-phonon interaction in Ca_2RuO_4 as a function of temperature between 10 K and

TABLE I: Site symmetries and IR's of the atoms in Ca_2RuO_4 with space group $\text{Pbca}-D_{2h}^{15}$. Mode classifications are: $\Gamma_{\text{Raman}} = 9 (A_g + B_{1g} + B_{2g} + B_{3g})$, $\Gamma_{\text{infrared}} = 11 (B_{1u} + B_{2u} + B_{3u})$, $\Gamma_{\text{silent}} = 12 A_u$, and $\Gamma_{\text{acoustic}} = B_{1u} + B_{2u} + B_{3u}$. The corresponding polarization tensor elements for each of the Raman-active factor group species are: $A_g \rightarrow \alpha_{xx}, \alpha_{yy}, \alpha_{zz}$; $B_{1g} \rightarrow \alpha_{xy}, \alpha_{yx}$; $B_{2g} \rightarrow \alpha_{xz}, \alpha_{zx}$; and $B_{3g} \rightarrow \alpha_{yz}, \alpha_{zy}$.

Atom	Site symmetry	IR's
Ru	C_i	$3 (A_u + B_{1u} + B_{2u} + B_{3u})$
Ca	C_1	$3 (A_g + B_{1g} + B_{2g} + B_{3g} + A_u + B_{1u} + B_{2u} + B_{3u})$
O(1)	C_1	$3 (A_g + B_{1g} + B_{2g} + B_{3g} + A_u + B_{1u} + B_{2u} + B_{3u})$
O(2)	C_1	$3 (A_g + B_{1g} + B_{2g} + B_{3g} + A_u + B_{1u} + B_{2u} + B_{3u})$

300 K.

II. EXPERIMENT

A single-crystal sample of Ca_2RuO_4 , which was grown by a floating-zone method,^{2,16,23} was mounted inside a continuous He-flow cryostat. The 647.1-nm excitation wavelength from a Kr-ion laser was used in a backscattering geometry with the propagation vector (\mathbf{k}) oriented along the c axis of the sample, $\mathbf{k} \parallel c$ -axis. Scattered light from the sample was dispersed using a triple-stage spectrometer, and then recorded using a liquid-nitrogen-cooled charge-coupled device (CCD) detector. Various polarization configurations of the incident and scattered light were employed in order to identify the scattering symmetries of the Raman spectra obtained for Ca_2RuO_4 : $(\mathbf{E}_i, \mathbf{E}_s) = (x, y)$, B_{1g} symmetry; $(\mathbf{E}_i, \mathbf{E}_s) = (x, x)$, A_g symmetry; and $(\mathbf{E}_i, \mathbf{E}_s) = (x', x')$, $B_{1g} + A_g$ symmetry, where \mathbf{E}_i and \mathbf{E}_s are the incident and the scattered polarization directions, respectively, B_{1g} and A_g are irreducible representations (IR's) of the space group D_{2h} , and $x \parallel [1,0,0]$, $y \parallel [0,1,0]$, and $x' \parallel [1,1,0]$. All the Raman spectra were corrected, first, by removing the CCD dark current response, and second, by normalizing the spectrometer response using a calibrated white light source. Finally, the corrected spectra were divided by the Bose thermal factor, giving rise to the spectral responses displayed in this paper. These responses are proportional to the imaginary part of the Raman susceptibility.

III. RESULTS AND DISCUSSION

Ca_2RuO_4 has an orthorhombic crystal structure (space group $\text{Pbca}-D_{2h}^{15}$) with four formula units per unit cell. A factor-group analysis, summarized in Table I, yields a total of 81 Γ -point phonons, of which 36 [$9 (A_g + B_{1g} + B_{2g} + B_{3g})$] are Raman-active modes involving Ca, in-plane oxygen [O(1)], and apical oxygen [O(2)] ions, 33 [$11(B_{1u} + B_{2u} + B_{3u})$] are infrared-active modes, and 12 ($12 A_u$) are silent modes. The Ru ions are located at a center of inversion symmetry and, thus, do not participate in any Raman-active phonon modes. Unlike tetragonal Sr_2RuO_4 , in which $2 A_{1g}$ and $2 E_g$ symmetry optical

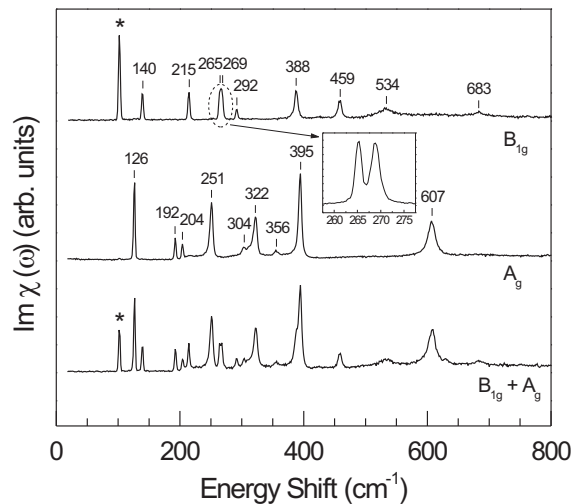


FIG. 1: Polarized Raman spectra at $T = 10$ K with B_{1g} , A_g , and $B_{1g} + A_g$ scattering symmetries from top to bottom, respectively. The inset shows a high-resolution Raman spectrum, indicating two resolved 265 and 269 cm^{-1} phonon modes.

phonons are Raman-active, orthorhombic Ca_2RuO_4 exhibits numerous phonon lines. This reflects the fact that substitution of Ca for Sr strongly distorts the RuO_6 octahedra, causing a rotation of the octahedra around the c axis, and a tilt of the octahedra around an axis on the RuO_2 plane.^{13,17} As shown in Fig. 1, polarized Raman spectra in a backscattering geometry (with the propagation vector $\mathbf{k} \parallel c$ -axis) reveal all of the phonon modes corresponding to each of scattering symmetries: 9 B_{1g} symmetry modes in $(\mathbf{E}_i, \mathbf{E}_s) = (x, y)$, 9 A_g symmetry modes in $(\mathbf{E}_i, \mathbf{E}_s) = (x, x)$, and 9 $B_{1g} + 9 A_g$ symmetry modes in $(\mathbf{E}_i, \mathbf{E}_s) = (x', x')$ polarization configurations, respectively. Note in the inset of Fig. 1 that the B_{1g} phonon peak energies assigned at 265 and 269 cm^{-1} are clearly resolved in a high-resolution Raman spectrum. More specific assignments of the observed optical phonons to particular atomic normal modes will require lattice dynamic

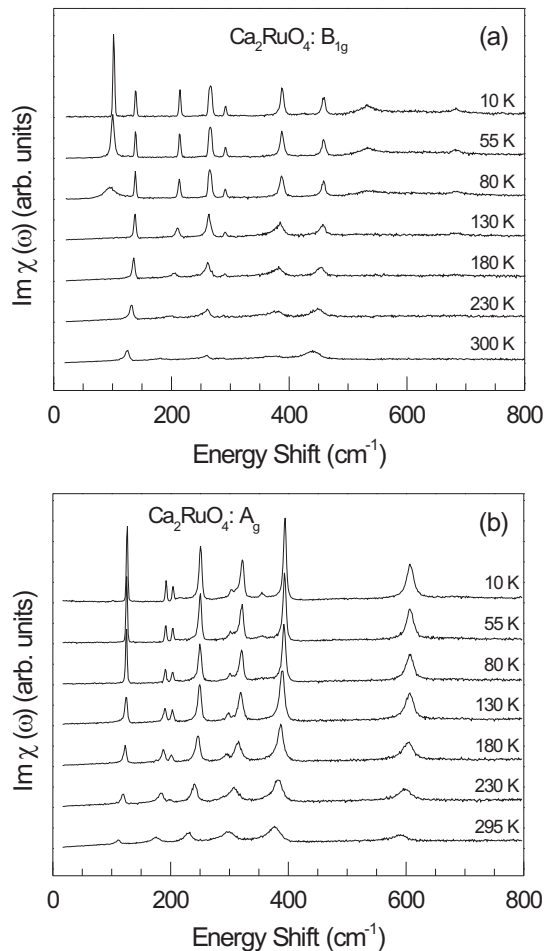


FIG. 2: (a) B_{1g} and (b) A_g Raman spectra with increasing temperature from 10 K to room temperature.

calculations.

Figure 1 also shows a Raman-active mode at 102 cm^{-1} (denoted with an asterisk) that is observed only in the B_{1g} scattering geometry. This mode is likely associated with a 2M scattering response, although we cannot completely rule out the possibility that it is a one-magnon excitation. The 2M scattering response, which involves a photon-induced flipping of spins on nearest-neighbor Ru sites, provides useful information concerning the AF correlations.^{9,10,24,25} Using the fact that the 2M energy for an $S = 1$ AF insulator is given by $\hbar\omega = 6.7 J$,²⁵ where J is the in-plane exchange coupling constant between nearest-neighbor Ru- $4d^4$ sites, we can estimate $J = 15.2 \text{ cm}^{-1}$ in Ca_2RuO_4 . With increasing temperature toward T_N , as shown in Fig. 2(a), the 2M response weakens in intensity, broadens in linewidth, and shifts to lower energy, reflecting the reduction of the AF correlations in Ca_2RuO_4 as the temperature is increased to

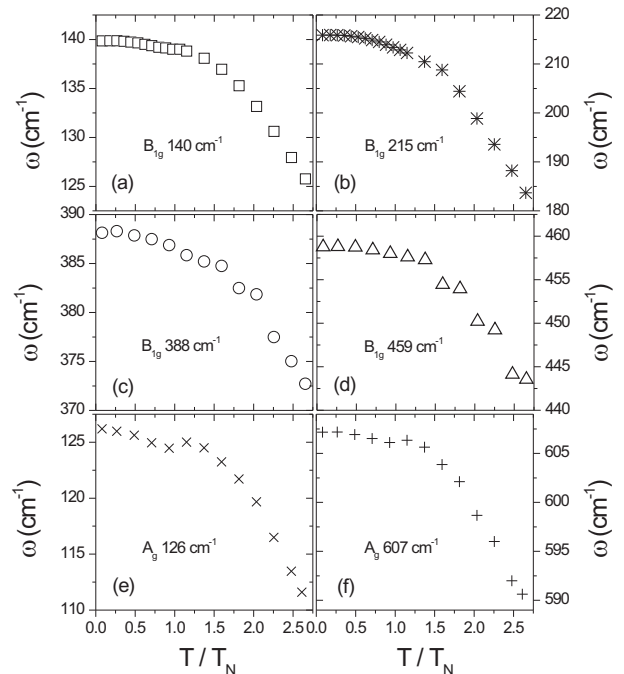


FIG. 3: Temperature-dependent frequency shifts of B_{1g} modes at (a) 140, (b) 215, (c) 388, (d) 459 cm^{-1} , and of A_g modes at (e) 126 and (f) 607 cm^{-1} .

T_N . Unlike the cuprates, the 2M scattering intensity in Ca_2RuO_4 diminishes rapidly above T_N , indicating that local AF order disappears for $T > T_N$. More details of the 2M characteristics in $\text{Ca}_{2-x}\text{Sr}_x\text{RuO}_4$ have been described elsewhere, including the effects of pressure⁹ and Sr substitution.¹⁰

With increasing temperature toward T_{MI} , the out-of-plane Ru-O(2) bond length is nearly unchanged for $T < T_N$, but gradually elongates as temperature is raised above T_N .^{13,17} In order to elucidate the temperature-dependence of the lattice parameters and the electron-phonon interaction below T_{MI} , both B_{1g} and A_g symmetry Raman spectra from Ca_2RuO_4 were studied as a function of increasing temperature from 10 to 300 K, as summarized in Figs. 2(a) and 2(b). There are several key features observed in the Raman spectra as a function of increasing temperature, including (i) a softening of all the B_{1g} and the A_g optical phonon energies, (ii) a decrease of phonon spectral weights, and (iii) a significant broadening and increased asymmetry of phonon lineshapes across T_N .

The systematic shifts of phonon peaks to lower energies with increasing temperature through T_N primarily reflect an elongation of the RuO_6 octahedra along the c axis. Figures 3(a) to 3(f) summarize the phonon energy changes with increasing temperature for some representative B_{1g} (140, 215, 388, and 459 cm^{-1}) and A_g (126 and 607 cm^{-1}) optical phonon modes. The phonon-

energy shifts are negligible for $T < T_N$, indicating little or no change in the lattice parameters in this temperature regime. In contrast, remarkable phonon-energy shifts are observed for $T > T_N$. Most of phonon modes display downward shifts of $\sim 15 \text{ cm}^{-1}$ as temperature is raised from 10 to 300 K. Interestingly, the B_{1g} phonon at 215 cm^{-1} shows a much more dramatic energy shift of $\sim 30 \text{ cm}^{-1}$. These Raman results are consistent with neutron scattering measurements, which show that there is little change in the lattice parameters for $T < T_N$, but that there is a significant change in the lattice parameters for $T_N < T \sim T_{MI}$.^{13,17} All the other B_{1g} and A_g optical phonons decrease in energy with increasing temperature. Note that all the B_{1g} phonon modes exhibit a dramatic decrease in intensity as temperature is raised toward T_{MI} ($\sim 357 \text{ K} \sim 3.2 T_N$), possibly reflecting increased damping of the modes by thermally activated carriers.

One notes in Figs. 2(a) and 2(b) that the B_{1g} and the A_g phonon lineshapes at low temperatures for $T < T_N$ are quite symmetric and narrow. In contrast, with increasing temperature through T_N , the phonon linewidths broaden significantly and the lineshapes become increasingly asymmetric. The latter reveals a Fano effect, caused by the interaction between the discrete phonon state and a broad electronic continuum of states.²⁶ Similar behavior has been observed in Raman spectra of numerous other strongly correlated materials such as $\text{Ca}_{2-x}\text{Sr}_x\text{RuO}_4$,¹⁰ $\text{La}_{1-x}\text{Ca}_x\text{MnO}_3$,²⁷ $\text{Ca}_3\text{Ru}_2\text{O}_7$,²⁸ Sr_2RuO_4 ,²⁹ and $R\text{TiO}_3$ ($R = \text{rare earth}$).²²

To study the temperature-dependence of the electron-phonon interaction in Ca_2RuO_4 in detail, the temperature-dependence of the phonon linewidths and asymmetries of the B_{1g} and A_g phonon modes were extracted by fitting these modes to a Fano lineshape, $I(\omega) = I_0(q + \epsilon)^2 / (1 + \epsilon^2)$, where $\epsilon = (\omega - \omega_0) / \Gamma$, ω_0 is the phonon energy, Γ is the effective phonon linewidth, and q is the asymmetry parameter. In this way, one obtains information on the electron-phonon interaction. The inverse of the asymmetry parameter, $1/|q|$, is proportional to the electron-phonon coupling strength V and the imaginary part of the electronic susceptibility ρ according to $1/q \sim V\rho$.^{10,26,27} Moreover, the electron-phonon coupling contribution to the phonon linewidth can be estimated from the fractional change in the phonon damping rate below T_{MI} , $[\Gamma(T) - \Gamma(RT)] / \omega_0 = \Delta\Gamma / \omega_0 \propto N(0)\omega_0\lambda$, where $N(0)$ is the electronic density of states at the Fermi surface, ω_0 is the phonon energy, and λ is the dimensionless electron-phonon coupling parameter.^{30,31,32} The parameter λ is related to the BCS parameter $N(0)V_{ph}$, where V_{ph} is the pairing potential arising from the electron-phonon interaction.^{31,32,33} Therefore, by carefully monitoring the phonon linewidths, as well as the inverse asymmetry parameters, as a function of temperature, one can obtain useful information regarding the evolution of the electronic density of states and the electron-phonon coupling strengths in Ca_2RuO_4 .

The role of the electronic contribution to the system

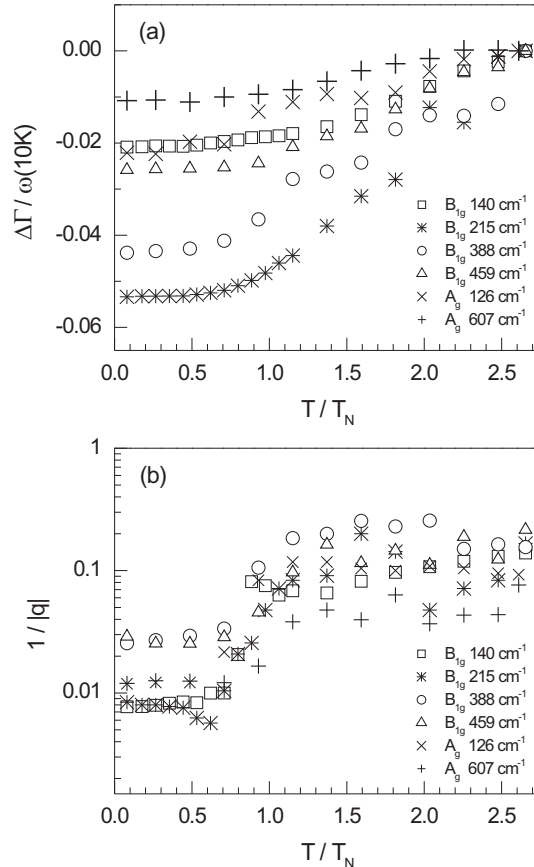


FIG. 4: (a) Phonon linewidth changes divided by the corresponding phonon energy at $T = 10 \text{ K}$, $[\Gamma(T) - \Gamma(RT)] / \omega(10 \text{ K}) = \Delta\Gamma / \omega(10 \text{ K})$, as a function of temperature normalized to T_N . (b) Magnitudes of inverse of the asymmetry parameters, $1/|q|$, as a function of temperature normalized to T_N .

above T_N , which influences the substantial phonon energy renormalizations observed above T_N , can be explored by plotting as a function of temperature the phonon linewidth changes divided by the corresponding phonon energy at $T = 10 \text{ K}$, $\Delta\Gamma / \omega(10 \text{ K})$. These plots are displayed in Fig. 4(a). Interestingly, in contrast to the negligible change in phonon linewidths observed below T_N , there is significant broadening in the phonon linewidths above T_N . For example, the phonon linewidths at 300 K are significantly broader than those at 10 K , $\Delta\Gamma / \omega_0 \sim 5.3 \%$, which is even larger than the fractional broadening observed in the correlation gap material FeSi , $\Delta\Gamma / \omega_0 \sim 3.5 \%$.³⁰ We attribute the systematic broadening of the phonon linewidths with increasing temperature above T_N to an increase of the effective number of electrons in the system for $T > T_N$. Indeed, Jung et al. recently reported that the effective number of electrons systematically increases, and the optical gap closes, with increasing temperature above T_N in Ca_2RuO_4 .⁷

The evolution of the electron-phonon interaction in Ca_2RuO_4 can be carefully illustrated by plotting the inverse of the asymmetry parameter, $1/|q|$, for different modes as a function of temperature, as shown in Fig. 4(b). Note that the magnitudes of the inverse asymmetry parameters, $1/|q|$, which are obtained from the representative B_{1g} and the A_g phonon modes, are negligible at low temperatures, but increase significantly as temperature is raised through T_N . Even when the temperature is much lower than the MI transition temperature, there is no additional increase of the inverse asymmetry parameters for $T/T_N > \sim 1.2$. These results strongly suggest that the largest increase in the electron-phonon coupling strength occurs near T_N , rather than near T_{MI} . By contrast, between $x = 0.45$ and 0.76 in $\text{La}_{1-x}\text{Ca}_x\text{MnO}_3$, the $1/|q|$ value decreases linearly with increasing x in the ferromagnetic low-temperature metallic region ($x \leq 0.52$), and vanishes in the AF region (for $x > 0.52$).²⁷ Note also that the magnitudes of the inverse asymmetry parameters, $1/|q|$, in the PM insulating region of Ca_2RuO_4 for $T_N < T < T_{\text{MI}}$ are comparable to those in the metallic region of Sr_2RuO_4 (Ref. 29) and $\text{La}_{1-x}\text{Ca}_x\text{MnO}_3$.²⁷

It is interesting to note that previous Raman results on $\text{Ca}_{2-x}\text{Sr}_x\text{RuO}_4$ have revealed that substitution of Sr for Ca increases the electron-phonon coupling strength, as evidenced by an increase of both the inverse asymmetry parameters and the phonon linewidths with Sr substitution at $T = 10$ K.¹⁰ Moreover, for the Sr-substituted samples ($x = 0.06$ and 0.09), a charge gap observed at 10 K was found to close well below the MI transition temperature, suggesting that the intermediate temperature regime between T_N and T_{MI} consists of a coexistence of insulating S-Pbca and metallic L-Pbca phases.¹⁰ In contrast, in this study, the broadening of phonon linewidths and the increase of the $1/|q|$ values upon heating through T_N ($\ll T_{\text{MI}}$) in Ca_2RuO_4 are probably not attributable to the coexistence of metallic and insulating phases in this temperature regime for several reasons, including the high stoichiometry of the sample, and the absence of any residual low frequency conductivity in Ca_2RuO_4 in the temperature regime $T_N < T < T_{\text{MI}}$.^{6,7}

In Ca_2RuO_4 , the observed increase in both the electron-phonon coupling strength and the number of effective carriers with increasing temperature near T_N strongly suggests that enhanced orbital fluctuations,

which are associated with increased electron transfer between the d_{xy} and $d_{yz/zx}$ orbitals, are responsible for the behavior observed in this temperature regime. Indeed, a recent O 1s x-ray absorption spectroscopy study of $\text{Ca}_{2-x}\text{Sr}_x\text{RuO}_4$ ($x = 0.0$ and 0.09) has suggested that orbital fluctuations gradually increase upon heating even in the insulating region well below T_{MI} .³⁴ Note that the inverse asymmetry parameters and the spectral linewidths for the phonon mode near 300 cm^{-1} in the insulating $RTiO_3$ ($R = \text{Gd, Sm, Nd, Pr, Ce, La}$) exhibit the largest values in LaTiO_3 ,²² suggesting that orbital fluctuations are important in LaTiO_3 , as pointed out by Keimer et al.²¹

IV. CONCLUSIONS

In summary, temperature-dependent Raman spectra of Ca_2RuO_4 allow us to explore the lattice dynamics near the MI transition temperature of this system. With increasing temperature through the Néel temperature, the B_{1g} and the A_g phonon modes exhibit a substantial shift to lower energies. Moreover, the phonons significantly broaden and exhibit increasingly asymmetric lineshapes upon heating in the vicinity of T_N . These results demonstrate that both the electron-phonon coupling strength and the effective number of electrons increase as temperature is raised through T_N , suggesting that orbital fluctuations are present in the PM insulating region in the temperature regime $T_N < T < T_{\text{MI}}$.

Acknowledgments

Work in Korea was supported by Korea Research Foundation Grant (KRF-2004-005-C00003). Work in Illinois was supported by the National Science Foundation under Grant No. DMR02-44502 and by the Department of Energy through the Materials Research Laboratory under Grant No. DEFG02-91ER45439. The work at Kyoto Univ. was supported in part by Grants-in-Aid for Scientific Research from JSPS and for the 21st Century COE ‘‘Center for Diversity and Universality in Physics’’ from MEXT of Japan.

¹ Y. Maeno, H. Hashimoto, K. Yoshida, S. Nishizaki, T. Fujita, J.G. Bednorz, and F. Lichtenberg, *Nature (London)* **372**, 532 (1994).

² S. Nakatsuji and Y. Maeno, *Phys. Rev. Lett.* **84**, 2666 (2000); S. Nakatsuji and Y. Maeno, *Phys. Rev. B* **62**, 6458 (2000).

³ T. Hotta and E. Dagotto, *Phys. Rev. Lett.* **88**, 17201 (2002).

⁴ S. Nakatsuji, D. Hall, L. Balicas, Z. Fisk, K. Sugahara,

M. Yoshioka, and Y. Maeno, *Phys. Rev. Lett.* **90**, 137202 (2003).

⁵ V.I. Anisimov, I.A. Nekrasov, D.E. Kondakov, T.M. Rice, and M. Sigrist, *Eur. Phys. J. B* **25**, 191 (2002).

⁶ J.S. Lee, Y.S. Lee, T.W. Noh, S.-J. Oh, J. Yu, S. Nakatsuji, H. Fukazawa, and Y. Maeno, *Phys. Rev. Lett.* **89**, 257402 (2002).

⁷ J.H. Jung, Z. Fang, J.P. He, Y. Kaneko, Y. Okimoto, and Y. Tokura, *Phys. Rev. Lett.* **91**, 56403 (2003).

- ⁸ T. Mizokawa, L. H. Tjeng, G. A. Sawatzky, G. Ghiringhelli, O. Tjernberg, N. B. Brookes, H. Fukazawa, S. Nakatsuji, and Y. Maeno, *Phys. Rev. Lett.* **87**, 77202 (2001).
- ⁹ C.S. Snow, S. L. Cooper, G. Cao, J.E. Crow, H. Fukazawa, S. Nakatsuji, and Y. Maeno, *Phys. Rev. Lett.* **89**, 226401 (2002).
- ¹⁰ H. Rho, S.L. Cooper, S. Nakatsuji, H. Fukazawa, and Y. Maeno, *Phys. Rev. B* **68**, 100404(R) (2003).
- ¹¹ S. Nakatsuji, V. Dobrosavljević, D. Tanasković, M. Minakata, H. Fukazawa, and Y. Maeno, *Phys. Rev. Lett.* **93**, 146401 (2004).
- ¹² K. Ishida, H. Mukuda, Y. Kitaoka, Z.Q. Mao, H. Fukazawa, and Y. Maeno, *Phys. Rev. B* **63**, 60507(R) (2001).
- ¹³ O. Friedt, M. Braden, G. André, P. Adelman, S. Nakatsuji, and Y. Maeno, *Phys. Rev. B* **63**, 174432 (2001).
- ¹⁴ S. Nakatsuji, S. Ikeda, and Y. Maeno, *J. Phys. Soc. Jpn.* **66**, 1868 (1997).
- ¹⁵ C.S. Alexander, G. Cao, V. Dobrosavljevic, S. McCall, J.E. Crow, E. Lochner, and R.P. Guertin, *Phys. Rev. B* **60**, 8422(R) (1999).
- ¹⁶ H. Fukazawa, S. Nakatsuji, and Y. Maeno, *Physica B* **281&282**, 613 (2000).
- ¹⁷ M. Braden, G. André, S. Nakatsuji, and Y. Maeno, *Phys. Rev. B* **58**, 847 (1998).
- ¹⁸ K.H. Kim, J.Y. Gu, H.S. Choi, G.W. Park, and T.W. Noh, *Phys. Rev. Lett.* **77**, 1877 (1996).
- ¹⁹ V.B. Podobedov, A. Weber, D.B. Romero, J.P. Rice, and H.D. Drew, *Phys. Rev. B* **58**, 43 (1998).
- ²⁰ S. Nimori, S. Sakita, F. Nakamura, T. Fujita, H. Hata, N. Ogita, and M. Udagawa, *Phys. Rev. B* **62**, 4142 (2000).
- ²¹ B. Keimer, D. Casa, A. Ivanov, J.W. Lynn, M.v. Zimmermann, J.P. Hill, D. Gibbs, Y. Taguchi, and Y. Tokura, *Phys. Rev. Lett.* **85**, 3946 (2000).
- ²² M. Reedyk, D.A. Crandle, M. Cardona, J.D. Garrett, and J.E. Greedan, *Phys. Rev. B* **55**, 1442 (1997).
- ²³ S. Nakatsuji and Y. Maeno, *J. Solid State Chem.* **156**, 26 (2001).
- ²⁴ P.A. Fleury and R. Loudon, *Phys. Rev.* **166**, 514 (1968); P.A. Fleury and H.J. Guggenheim, *Phys. Rev. Lett.* **24**, 1346 (1970).
- ²⁵ S. Sugai, M. Sato, T. Kobayashi, J. Akimitsu, T. Ito, H. Takagi, S. Uchida, S. Hosoya, T. Kajitani, and T. Fukuda, *Phys. Rev. B* **42**, 1045 (1990).
- ²⁶ U. Fano, *Phys. Rev.* **124**, 1866 (1961).
- ²⁷ S. Naler, M. Rubhausen, S. Yoon, S.L. Cooper, K. H. Kim, and S.W. Cheong, *Phys. Rev. B* **65**, 92401 (2002).
- ²⁸ H.L. Liu, S. Yoon, S.L. Cooper, G. Cao, and J.E. Crow, *Phys. Rev. B* **60**, R6980 (1999).
- ²⁹ S. Sakita, S. Nimori, Z.Q. Mao, Y. Maeno, N. Ogita, and M. Udagawa, *Phys. Rev. B* **63**, 134520 (2001).
- ³⁰ P. Nyhus, S.L. Cooper, and Z. Fisk, *Phys. Rev. B* **51**, 15626 (1995).
- ³¹ P.B. Allen, *Phys. Rev. B* **6**, 2577 (1972).
- ³² J.D. Axe and G. Shirane, *Phys. Rev. Lett.* **30**, 214 (1973).
- ³³ W.L. McMillan, *Phys. Rev.* **167**, 331 (1968).
- ³⁴ T. Mizokawa, L.H. Tjeng, H.-J. Lin, C.T. Chen, S. Schuppler, S. Nakatsuji, H. Fukazawa, and Y. Maeno, *Phys. Rev. B* **69**, 132410 (2004).